Combined capacitive and electrochemical charge storage mechanism in high-performance graphene-based lithium-ion batteries

Combined capacitive and electrochemical charge storage mechanism in high performance graphene-based lithium-ion batteries

Silvio Scaravonati(a), Michele Sidoli(a), Giacomo Magnani(a), Alberto Morenghi(a), Marcello Canova(b), Jung-Hyun Kim(b), Mauro Riccò(a), Daniele Pontiroli(a).*

(a) Nanocarbon Laboratory, INSTM & Department of Mathematical, Physical and Computer Sciences, University of Parma, Parco Area delle Scienze 7/A, 43124, Parma, Italy;

(b) Center for Automotive Research, The Ohio State University, 930 Kinnear Road, 43212, Columbus, Ohio, USA.

**Corresponding author. Email address: daniele.pontiroli@unipr.it*

Abstract

Improvements in Li-ion battery technology can be achieved by developing novel, high-performance electrode materials. Graphene appears to be a good candidate as an anode material for Li-ion batteries thanks to the similarity with graphite, the good electrical conductivity, the ability to achieve fast charge and discharge cycles, and the higher capability to host lithium ions. Our previous studies demonstrate the capability of intercalating lithium in graphene-based electrodes with a high specific capacity of 500 mA h g^{-1} at C/5 current. In this study, graphene, synthesized through scalable thermal exfoliation of graphite oxide, and hydrogenated graphene is employed to assemble optimized Li-ion half-cells, which are systematically characterized by means of electrochemical measurements. Hydrogenated graphene boasts an impressive reversible specific capacity with fast charge/discharge capabilities, exceeding 370 mA h g^{-1} even at 25 C-rate. Diffusion mechanisms of lithium is characterized at different states of intercalation by means of electrochemical impedance spectroscopy. In addition, a novel combined electrostatic and electrochemical charge storage mechanism of lithium ions in graphene-based electrodes is proposed, based on three-electrode cyclic voltammetry investigation. Furthermore, graphene and hydrogenated graphene anodes are paired with commercial cathode materials, to study the feasibility of their application to full-cells.

Keywords: Lithium-ion batteries, graphene and hydrogenated graphene, lithium diffusion, intercalation mechanism, full-cells.

---

1. Introduction

Lithium-ion batteries (LIBs) have been attracting considerable attention as an environment-friendly power supply. One of the reasons for the fast growth of LIBs is their capability of high performance and high specific energy. They amount now to 63% of world rechargeable battery market [1], corresponding to annual sales of over 7 billion dollars [2]. The most promising application for lithium-ion technology is to electric propulsion, thanks to their top performance and relatively low weight, compared to other battery technologies. Despite the good performance, LIBs still face challenges, due to high costs, short lifespan, and more importantly low energy density. Specific energy of fossil fuels is about 1300-1600 W h kg^{-1}, while best LIBs have a specific energy up to 240 W h kg^{-1} [3,4]; the development of more performing batteries is then crucial to obtain a more widespread diffusion of electric cars.

Carbon nanostructures are good candidates as anode materials alternative to graphite in energy storage devices, due to their unique properties, such as high specific surface area [5–8], good electrical conductivity [9,10] and capability of hosting alkali and alkali-earth ions [11–14]. Among the many carbon nanostructures, graphene demonstrated to be a promising negative electrode material for LIBs [15,16], and graphene-related materials have been reported to achieve high specific capacities, up to 1200 mA h g^{-1} [9]. Graphene is a single layer of carbon atoms in a two-dimensional hexagonal honeycomb-like lattice. It can be considered the basic constituent of graphite. Graphene features a very good electrical conductivity and an outstanding specific surface area [17–19] and it is currently a good candidate as electrode material for energy storage devices such as batteries and supercapacitors. Graphene has already been used to increase specific capacity of batteries and maximum rate of charge and discharge; thanks to its affinity with graphite, batteries with graphene-based anodes can be assembled easily by partially exploiting the already established LIB technology. The possibility of realizing graphene-based full-cells with $LiFePO_4$ cathodes has been reported before [20]. Moreover, graphene is also a good candidate in composite materials, in conjunction with high-capacity lithium-ion cathodes or anodes, as a conductive matrix [21–24].

Despite the promising properties of graphene in LIBs, some problems have yet to be solved before its commercial use. The main issue is a large first-cycle irreversibility due to a massive Solid Electrolyte Interphase (SEI) formation, which requires a pre-lithiation process in order to avoid the complete exhaustion of lithium from the battery [18,20,25]. Another issue is that many different methods of synthesis have been proposed for graphene, and cost and material properties are strongly dependent on the synthesis method [17]. This leads to some difficulties in determining which method of synthesis is most suitable for each application, ranging from porous electrodes in supercapacitors, negative electrodes in batteries, or conductive matrix in composites [26]. Consequently, it is typically hard to find thorough investigations of the energy storage mechanisms in graphene-based active materials. In addition to this, the most widely used method for the oxidation of graphite, usually required for the mass-scale production of graphene, is the modified Hummers method [27], which yields difficult to dispose manganese-containing wastes.

Among the methods for graphene synthesis, thermal exfoliation of graphite oxide produced via the Brodie method is scalable and manganese-free [28]. Compared to other methods for the synthesis of graphene-related materials, this one has the advantage of being a top-down approach, which starts from graphite powder, hence it is more easily scalable than bottom-up approaches [29,30]. Moreover, it does not require further activation processes or doping with heteroatoms [31,32]. Former studies demonstrated capability of reversibly intercalating thermally exfoliated graphene and its

derivatives with lithium and sodium [18,33]. Sodium intercalation mechanism in graphene has also been already investigated in detail with nuclear magnetic resonance [34].

The aims of this study are to investigate lithium storage in graphene, and to increase performance of LIBs by exploiting the properties of carbon nanostructured materials. Graphene synthesized with a scalable method, which does not require the use of heavy metals during the synthesis process [35], was characterized as anode material in LIB, to better understand intercalation mechanisms and to develop novel technologies for LIBs. Prior studies suggest a possible combination of different charge storage mechanisms in graphene-based electrodes, but to the best of our knowledge such effect has never been studied in depth before [25]. Graphene was also subject to a hydrogenation process, to remove oxygen atoms and saturate defects, such as dangling bonds, produced during the synthesis process [35]. Moreover, graphene and hydrogenated graphene were integrated with suitable cathodes to develop complete cell prototypes, more similar to possible commercially viable products. For the first time, graphene produced by thermal exfoliation with a highly scalable method as well as its hydrogenated derivative were coupled to two different cathodes to realize lithium-ion full-cells.

2. Experimental

All samples preparation and cell assembly were performed in an argon-filled glove box (MBRAUN MB 200B and MBRAUN Labmaster 130), with oxygen and water concentrations lower than 1 ppm; electrochemical cells and solid electrolyte samples were tested in airtight stainless steel coin cells (CR2032).

2.1. Sample preparation

Thermally exfoliated graphite oxide (TEGO) was synthesized starting from graphite powder (SGL Carbon, RW-A grade, average particle size 66 μm), which was oxidized through the Brodie method: graphite was mixed with powdered sodium chlorate ($NaClO_3$, Sigma Aldrich, >99%); concentrated nitric acid was added dropwise under continuous stirring and temperature was kept close to 0 °C through an ice bath. The mixture was then heated for 8 h at 60 °C with a slow thermal ramp (20 °C h^{-1}). After cooling to room temperature, the mixture was stirred for 24 h, until it became dark green. The suspension was then washed in milli-Q water and filtered with a coarse filter paper; the product was then washed in a water-based hydrochloric acid solution, filtered, and washed again two more times with milli-Q water. The product was then dried at 60 °C overnight. The obtained graphite oxide powder was thermally exfoliated by sudden exposure to 1150 °C under dynamic vacuum, thus obtaining TEGO [18]. Such product has been extensively characterized in previous studies [28]. Hydrogenated TEGO (H-TEGO) was obtained by heating TEGO in a quartz vial at 800 °C under hydrogen flux for 1 h at ambient pressure. Neither TEGO or H-TEGO have been exposed to air during their preparation [18].

2.2. Structural Characterization

Precursor graphite, graphite oxide, TEGO and H-TEGO were characterized through powder X-ray diffraction (XRD), which was performed on a Bruker D8 Discover operating in Debye-Scherrer geometry, with a copper source (CuK_α radiation) and equipped with a Rayonix MX225 2D area detector. Samples were sealed in a glass capillary under argon atmosphere and rotated, thus reducing preferred orientations of crystallites during measurements.

Nitrogen adsorption-desorption analysis was performed at 77 K with a Coulter SA 3100 surface area and pore size analyzer. The total specific surface area was calculated with the Brunauer Emmett Teller (BET) method. The pore size distribution was evaluated with the Barrett-Joyner-Halenda (BJH) method, desorption branch.

2.3. Cell Preparation

TEGO-, H-TEGO and graphite-based electrodes (MTI Corporation, 99.5%, 19-23 μm mesh) were prepared by mixing 90% in weight of the active material with 10% polyacrylic acid (PAA, Sigma Aldrich, average Mw = 1800). Among the different binders we tested, including PAA, polyvinylidene fluoride (PVdF), sodium alginate, and carboxymethyl cellulose, PAA yielded the best results in terms of mechanical strength and electrochemical performance. No conductive agent was added because of the high electrical conductivity of the active materials [18]. Slurries were obtained by adding anhydrous N-methyl-pyrrolidone (NMP, Sigma Aldrich, 99.5%) until the solution was completely homogeneous, then the mixture was cast on a copper foil (Alfa Aesar, 10 μm thick, 99.8%) and spread with a thickness of 0.5 mm with a notch bar. NMP was slowly removed at 60 °C in air for 30 minutes, then at 80 °C in a vacuum oven overnight. Electrodes were then hot-pressed at 50 °C between two rollers with a spacing of 30-80 μm, depending on the thickness of the dried electrode, and punched with a diameter of 13.7 mm. Before cell assembly, mass and thickness of each electrode were measured. Typical mass loading was of about 2 mg for TEGO and 1 mg for H-TEGO.

Half-cells were assembled either to characterize TEGO and H-TEGO (in comparison with graphite), or to achieve pre-formation of the SEI on the graphene-based electrodes before assembling full-cells. Pre-formed graphene-based electrodes were tested in full-cells, in combination with different cathodes.

For both half-cells and full-cells, CR2032 coin cells were assembled starting by placing the electrodes at the bottom case. Then, a piece of Celgard 2500 separator was placed onto an electrode and soaked in the electrolyte, consisting of 1 M lithium hexafluorophosphate ($LiPF_6$) solution in ethylene carbonate (EC)/diethyl carbonate (DEC) with 1/1 vol. ratio (Merck corporation, battery grade). For half-cells, a lithium disk was cut from lithium ribbon (Sigma Aldrich, 99.9 %) and used as the counter electrode by placing it onto the wet separator.

For full-cells, two different types of cathodes were prepared by mixing 85% weight of $LiNi_{1/3}Mn_{1/3}Co_{1/3}O_2$ (NMC, Ni:Mn:Co=1:1:1) or $LiFePO_4$ (LFP) powder, with 7.5 % of carbon black (Timcal, Super P) conductive agent and 7.5 % of PVDF binder in anhydrous NMP. Solutions were stirred and cast on an aluminum foil and spread with a 0.3 mm notch bar. NMP was slowly removed at 60 °C in air for 30 minutes, then at 80 °C in a vacuum oven overnight, and electrodes were then punched with a diameter of 13.7 mm. Typical mass loading of the cathodes was of about 2 mg. In order to assemble the full-cells, TEGO and H-TEGO electrodes need to be treated with a process for the pre-formation of the SEI. Pre SEI formation is necessary to properly characterize the full-cell behavior without having to take into account the Li ion loss during the first cycle. Moreover, since a considerable amount of lithium is depleted during the formation of the SEI, the cathode would lack enough lithium to achieve complete lithiation of the anode during the subsequent cycles. To compensate such initial Li-loss during the SEI formation process, we pre-formed graphene-based anodes by following an electrochemical method. Half-cells with graphene-based electrodes were discharged and charged three times, followed by recovering the cycled electrodes. This electrochemical pre SEI formation method is different from previously reported

direct contact with a lithium foil [20], which has the disadvantage of an incomplete formation of the electrode, proven by the capacity loss during the first cycles, indicating that more than one cycle is preferable. Earlier studies reported an evidence that the SEI was preserved after disassembling the half-cells [34]. The recovered cycled electrodes were placed in new coin cells, together with a fresh Celgard separator and electrolyte, paired with the cathodes. The mass ratio of cathode and anode needs to be balanced with regard to their specific capacities, and the full-cells are assembled with a fully lithiated cathode and a lithium-empty anode. The cathode/anode ratio of the full-cells were targeted to be 1.0 with a tolerance of 10%.

2.4. Electrochemical measurements

Conductivity of TEGO and H-TEGO was measured by supplying different values of direct current, in the range of 10^{-3}-10^{-6} A, with a Keithley 6221 Current Source and measuring the direct voltage with a Keithley 2182A Nanovoltmeter. Measurements were made on thin samples, with four ohmic gold contacts in linear geometry with the Keithley Source and Nanovoltmeter operating in Delta mode.

Electrochemical impedance spectroscopy (EIS) measurements were performed on half-cells after three complete formation cycles, using a Gamry Interface 1010E potentiostat/galvanostat. An alternate current (AC) signal which corresponds to a 0.1 C-rate was applied, with frequencies ranging from 80 mHz to 200 KHz. For each frequency, data was acquired as |Z| and θ and averaged on 7 measurements. Diffusion coefficient for lithium ions was calculated from:

$$D = \frac{1}{2} V_m^2 \frac{\left(\frac{dE}{dx}\right)^2}{(FA\sigma)^2}$$

where V_m is the molar volume of the compound in which the charge is diffusing, dE/dx is the slope of the open circuit voltage curve, F is the Faraday constant, A is the interfacial area between the electrode and the electrolyte, and σ is the Warburg coefficient, which is the slope of the imaginary part of the impedance versus $\omega^{-1/2}$ [36]; linearity is shown in Figure S1. The molar volume V_m is assumed constant. This assumption is consistent with the fact that no volume changes in graphene-like materials have ever been reported to the best of our knowledge, and the most comparable anode material is graphite, in which only small volume expansion has been reported [37,38]. Such method has already been effectively employed to study lithium diffusion in graphite [39] and in nanomaterials [40]. For the interfacial area A, the geometric area of the electrode has been chosen, since common techniques employed to evaluate specific surface area, as Brunauer-Emmet-Teller (BET) technique, are ineffective in evaluating the interfacial area between the electrode and the electrolyte [41]. It is worth noting that the actual interfacial area of nanomaterials, as TEGO and H-TEGO, is typically larger than the geometric area; therefore, diffusion coefficient D has to be intended as an "apparent diffusion coefficient", as typically established for nanomaterials [42,43].

Cyclic voltammetry (CV) has been performed with a three-electrode configuration using a Keithley 2400 Multimeter. The measurement was performed in an argon-filled glove box, and a polypropylene Swagelok® T-tube was employed as a sample holder. TEGO-based electrodes, prepared with the same process employed for half-cells electrode, were used as working electrodes, while pure lithium (Sigma Aldrich, 99.9 %), was used as both counter electrode and reference electrode. Celgard foil was employed as a separator, and the T-tube was filled with $LiPF_6$ in EC/DEC electrolyte solution.

Stainless steel current collectors were employed for both the working and the counter electrodes, while the reference electrode was placed in an electrolyte-filled glass vial in contact with the T-tube electrolyte through a porous frit. CV measurements have been performed at voltage rates of 50 μV/s, 100 μV/s, 200 μV/s, 500 μV/s, 1 mV/s, 2 mV/s, 5 mV/s and 10 mV/s in a voltage window of 0.05 V – 2 V. The fraction of electrochemical and electrostatic contribution to capacity was evaluated by using the Dunn method. For a fully electrostatic contribution to capacity, current is a linear function of voltage rate, while for a fully electrochemical contribution, current is proportional to the square root of the voltage rate. The total current is a linear combination of the two contributions:

$$i = a \cdot v + b \cdot v^{1/2}$$

where v is the voltage rate, and a and b, the weights of each contribution to capacity, can be estimated by fitting the previous equation [44,45].

For galvanostatic chronopotentiometry (GCP), an Arbin LBT21084 battery test equipment was employed. The instrument potential values were sampled every 1 s. Half-cells were charged and discharged between 0.01 V and 2 V at different C-rates, with typical current densities of about 0.2 A g^{-1} for TEGO and 0.67 A g^{-1} for H-TEGO. Full-cells between 0.01 V and the maximum operation voltage of the cathodes: 4.4 V for NMC and 3.5 V for LFP.

3. Results and discussion

3.1. Characterization of TEGO and H-TEGO

The measurement of DC conductivity provided 9.4 ± 0.1 S cm^{-1} and 9.74 ± 0.04 S cm^{-1} for TEGO and H-TEGO, respectively. Both values allowed us to employ TEGO and H-TEGO as battery electrodes without the addition of any conductive agent. Precursor graphite, graphite oxide, TEGO and H-TEGO were characterized by means of powder XRD. The successful oxidation of graphite is proven by the shift of the main (002) peak at lower angles, corresponding to an increase in the distance between graphene planes (Figure S2). After exfoliation, crystallinity is reduced, and the (002) peak is widened, indicating a disordered structure in which TEGO flakes are characterized by a distribution of different number of graphene sheets (Figure S2). No changes are observed between the diffraction pattern of TEGO and that of H-TEGO.

Sorption analysis was performed both on TEGO. The sample displayed a BET specific surface area of 650 ± 20 m^2/g and a pore volume of 2.62 ± 0.02 mL/g. The isotherm obtained on TEGO is reported in Figure S3. BJH pore size distribution (Figures S4 (a) and S4 (b)) shows the presence of micro-, meso- and macropores. The pore size distribution shows that the most part of the pores has a diameter between 20 and 80 nm, while another smaller peak is present for pores < 6 nm.

Morphology of TEGO and H-TEGO, synthesized through the same method, has been previously characterized with transmission electron microscopy (TEM), scanning electron microscopy (SEM) and selected-area electron diffraction (SAED), demonstrating the presence of both single-layer and few-layer sp^2 carbon [28]. The majority of graphene sheets in TEGO are stacked in structures of mainly three layers with turbostratic disorder, as observed with X-ray photoelectron spectroscopy (XPS), ultraviolet photoelectron spectroscopy (UPS) [46] and neutron total scattering measurements [47].

High resolution TEM highlighted ordered domains of 10-15 nm; this was confirmed by Raman spectroscopy, in which the ratio between the integrated peak areas of the D and the G bands yielded an average size of the sp^2 domains of 12.3 nm. The presence of sp^3 carbon, observed with XPS and TEM images, is indicative of the presence of defects both on the graphene sheets and between sheets [28]. XPS also detected a carbon/oxygen ratio of 97.1%/2.8% by mass, due to the remaining functional groups that are not removed during the thermal exfoliation process. For H-TEGO, carbon/oxygen ratio is 96.9%/3.1%, meaning that during the hydrogenation process the oxygen containing functional groups attached to TEGO are approximatively unchanged [46]. On the other hand, previous inelastic neutron scattering (INS) studies, also supported by nuclear magnetic resonance (NMR), demonstrated that annealing TEGO in H_2 has the effect of increasing the fraction of hydrogen from 0.17% to 0.69% by mass [46]. It is worth noting that XPS detected, after hydrogenation, an increase of sp^2 carbon, from 68.9% to 73.2%, at the expense of sp^3 carbon, from 21.3% to 9.5% [46], probably indicating a decrease of the concentration of defects. The increase of the sp^2 carbon explains the slight increase of the electrical conductivity of TEGO after hydrogenation.

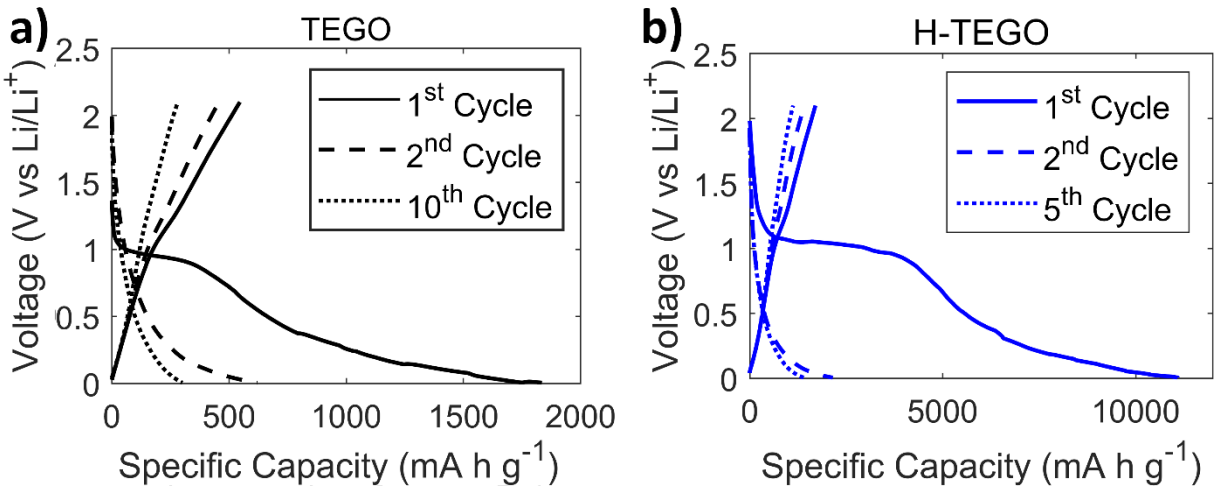

Figure 1. Voltage profiles of half-cells with electrodes based on (a) TEGO and (b) H-TEGO as a function of the specific capacity, measured with a low rate of charge (0.05 C for TEGO, 0.1 C for H-TEGO), for the first and subsequent cycles.

3.2. Galvanostatic Chronopotentiometry

The performance of lithium-ion half-cells with electrodes based on TEGO and H-TEGO were tested by means of galvanostatic chronopotentiometry (GCP), by discharging and charging the cells at different C-rates; a slow 0.1 C-rate was employed to have a good approximation of the open circuit voltage (OCV) curves, while faster C-rates were employed to study the fast charge and discharge capabilities of the electrodes. Both TEGO and H-TEGO are characterized by a different shape of the GCP curve between the first discharge and the subsequent ones. In particular, TEGO and H-TEGO electrodes are characterized by a single plateau at about 1 V during the first discharge, with a specific capacity exceeding 1500 mA h g^{-1} (Figure 1 (a)) for TEGO and 10000 mA h g^{-1} for H-TEGO (Figure 1 (b)), and subsequent cycles with a steeply decreasing discharge curve, characterized by the absence of plateaus, which is atypical for batteries (Figure 2). The reason for such differences lies in the fact that both TEGO and H-TEGO are characterized by a very large specific surface area, of about 500 m^2 g^{-1} [28], which relates to the interface between the electrode and the electrolyte. For this reason, the effect of the solid-electrolyte interphase (SEI) formation in TEGO or H-TEGO is more predominant than in conventional electrodes, and most of the specific capacity observed during the first cycle is not actually an intercalation

process; the 1 V plateau probably corresponds to the SEI formation reaction interface as evidenced by its irreversibility (i.e., absent from the 2nd cycle). The subsequent cycles are characterized by a steeply decreasing shape of the discharge potential curve, with a low potential as observed for graphite, the only difference lying in the fact that in graphite the potential suddenly drops to a low potential plateau. A lower specific capacity, with respect to the first cycle, is observed in the following cycles, although still higher than that of graphite. Even though a decrease of the specific capacity is observed not only after the first cycle, but for about the first 5 cycles, the absence of the SEI formation plateau observed during the first discharge suggests that the higher capacity attributed to the formation of the SEI is mainly limited to the first cycle. Consequently, the real specific capacity of TEGO and H-TEGO is that from the second cycle, and the specific capacity loss during the first 5 cycles is probably due a strong bonding between Li-ions and TEGO. TEGO delivered a specific capacity of about 304 ± 14 mA h g^{-1} after 5 cycles at 0.1 C-rate, which is similar to that of graphite electrode (Figure 2, Figure 3 (a)). It still delivered a specific capacity of 109 ± 3 mA h g^{-1} even at 25 C-rate, as shown in Figure 3 (a). In comparison, H-TEGO provided much higher capacity than TEGO: for example, H-TEGO delivered 1290 ± 60 mA h g^{-1} at 0.1 C-rate, and 360 ± 20 mA h g^{-1} at 25 C-rate. For the case of 1 C-rate, the observed specific capacity is 670 ± 40 mA h g^{-1} (Figure 3 (c)). Galvanostatic curves for TEGO and H-TEGO at different C-rates can be found, respectively, in Figure 3 (b) and Figure 3 (d). In Figure 3, for both TEGO and H-TEGO, the first cycle, dominated by the formation of the SEI layer, has been excluded.

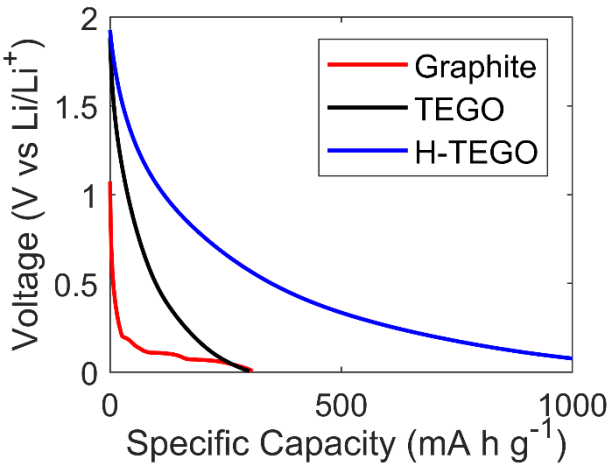

Figure 2. Comparison between voltage versus specific capacity of TEGO, H-TEGO and graphite.

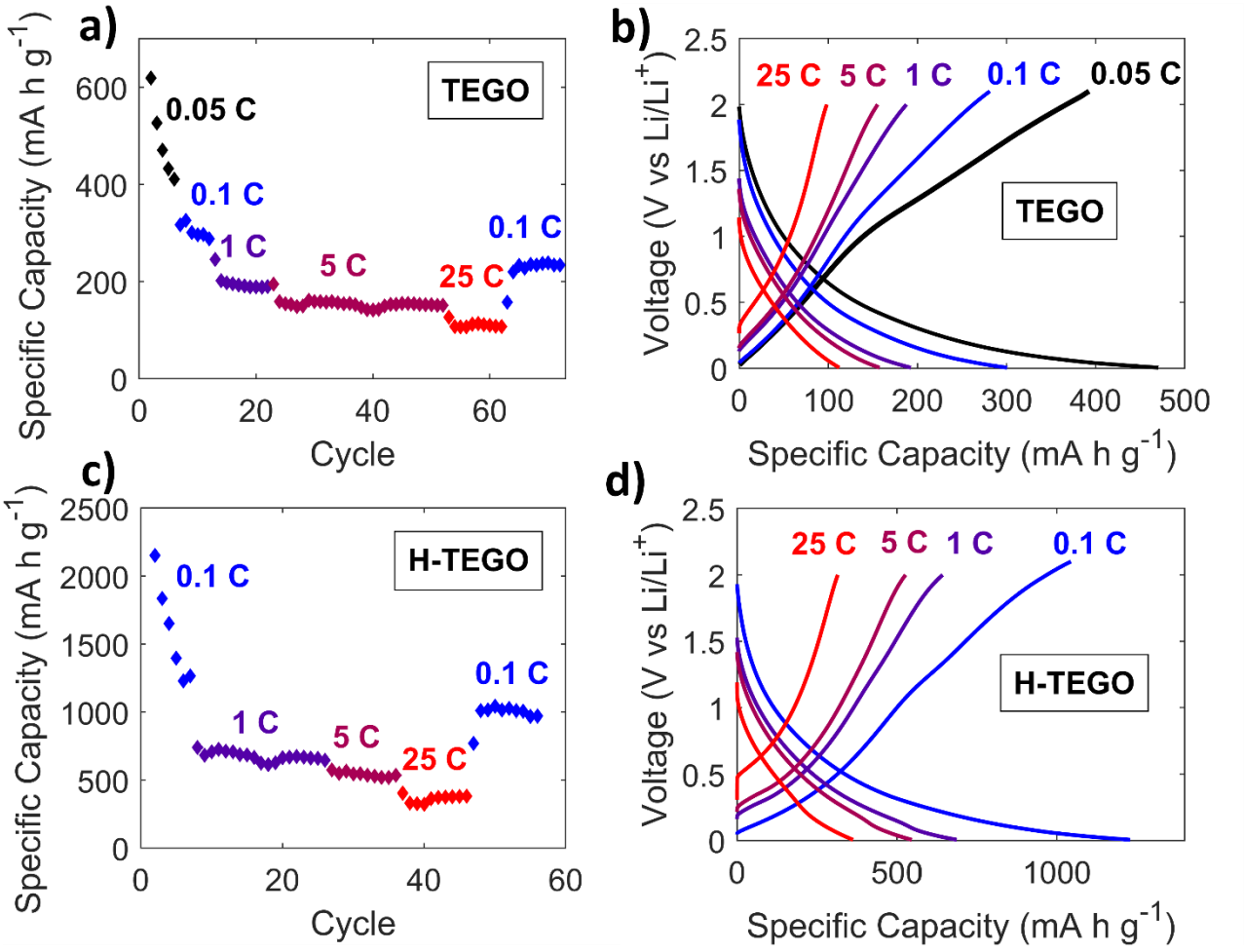

Figure 3. Comparison of discharge specific capacities at different C-rates for (a) TEGO and (c) H-TEGO. Voltage profiles of (b) TEGO and (d) H-TEGO.

3.3. Electrochemical Impedance Spectroscopy

EIS measurements on half-cells with electrodes based on TEGO and H-TEGO were performed at a constant temperature of 25 °C and at different SOC conditions. The EIS was measured at every 10% interval of the specific capacity during charging and discharging the cells with a steady current, in order to study diffusion dynamics in graphene-based electrodes at each stage of intercalation and explain the steeply decreasing behavior of the discharge GCP curve. EIS was performed after three charge and discharge cycles, to stabilize the contribution caused by the impedance of the SEI formation. Nyquist plots for EIS performed on TEGO, as a function of the content of lithium in the electrode, are shown in Figure S5 (a) for the lithiation (half-cell discharge) process and in Figure S5 (b) for the de-lithiation (half-cell charge) process, while Nyquist plots for lithiation and de-lithiation of H-TEGO are shown in Figures S5 (c) and (d), respectively. Diffusion coefficient of lithium in TEGO (Figure 4 (a)) and H-TEGO (Figure 4 (b)) has been calculated from EIS as a function of the content of lithium in the electrode. The equivalent circuit model for the system is shown in Figure S6. R_e is the high frequency series resistance, comprising the resistance of the electrolyte and the external resistance of the circuit, R_{ct} is the charge transfer resistance between the electrode and the electrolyte, Z_w is the Warburg impedance and CPE is the constant phase element impedance, considering the geometrical capacity of the system. Diffusion coefficient has been calculated from the Warburg coefficient and the voltage profile obtained from the GCP potential acquired before each EIS

measurement. During lithiation, diffusion coefficient is higher when the content of lithium in TEGO and H-TEGO is low, respectively of $8.4 \cdot 10^{-8}$ cm^2 s^{-1} and $5.6 \cdot 10^{-10}$ cm^2 s^{-1}, and it decreases continuously, down to $2.4 \cdot 10^{-9}$ cm^2 s^{-1} and $7.6 \cdot 10^{-12}$ cm^2 s^{-1}, as the lithium content increases, probably due to a hindrance to the lithium insertion caused by the ions that are already filling the electrode. During de-lithiation, a maximum in the diffusion coefficient is observed for a nearly full electrode, with peak diffusion respectively of $1.3 \cdot 10^{-7}$ cm^2 s^{-1} and $8.5 \cdot 10^{-10}$ cm^2 s^{-1}, as observed for graphite [48], possibly due to the fact that electrostatic repulsion of lithium in TEGO and H-TEGO promotes the release of lithium ions. At half state of lithiation, diffusion coefficient is nearly identical for lithiation and de-lithiation: for TEGO calculated diffusion coefficient is $1.8 \cdot 10^{-8}$ cm^2 s^{-1} (lithiation) and $2.3 \cdot 10^{-8}$ cm^2 s^{-1} (de-lithiation), while for H-TEGO calculated diffusion coefficient is $1.0 \cdot 10^{-10}$ cm^2 s^{-1} (lithiation) and $1.4 \cdot 10^{-10}$ cm^2 s^{-1} (de-lithiation). EIS has been performed also on graphite, and diffusion coefficient of graphite has been calculated as well, in order to allow a comparison between TEGO, H-TEGO and graphite (Figure 4 (c)).

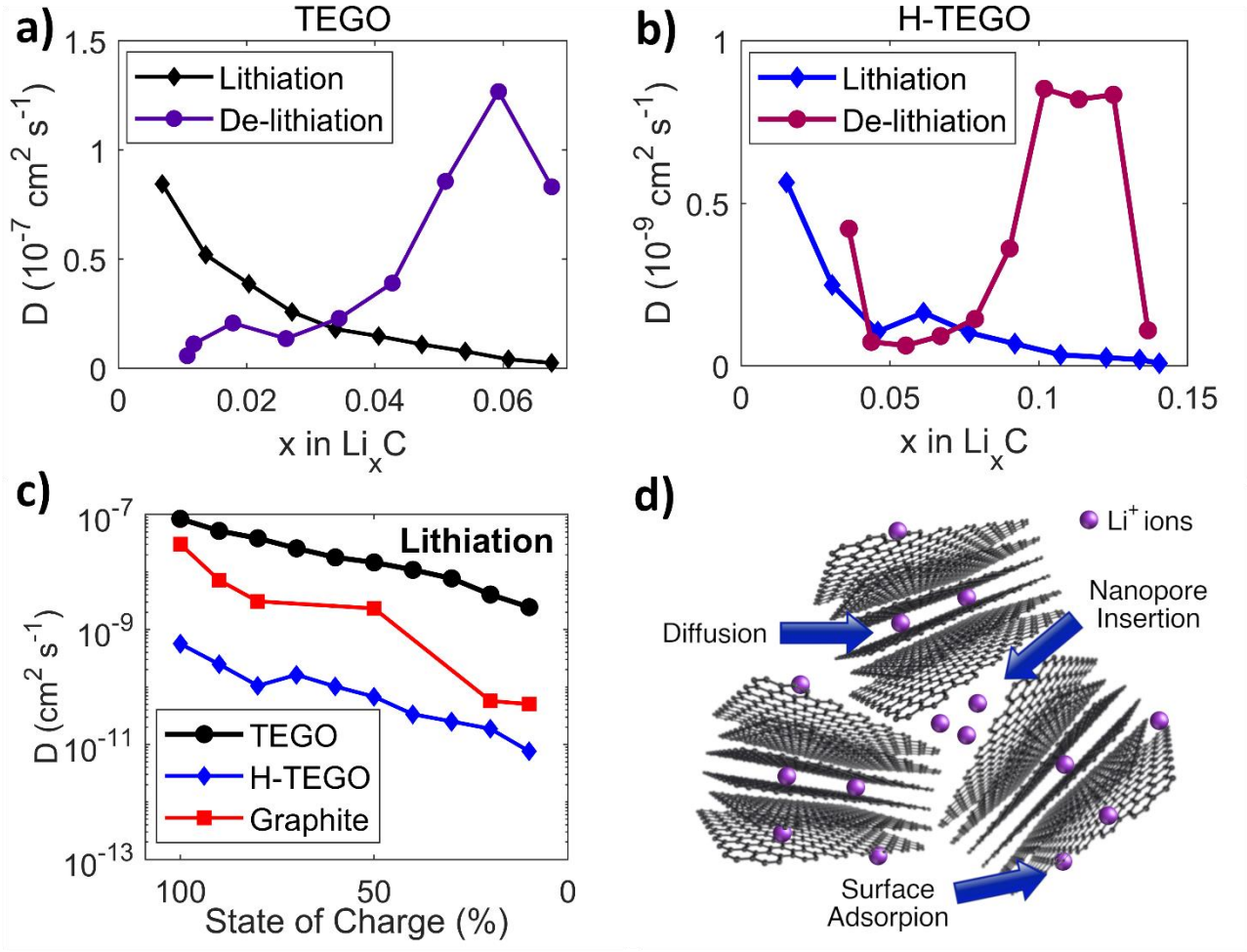

Figure 4. Diffusion coefficient of lithium in (a) TEGO and (b) H-TEGO, at different stages of lithiation and de-lithiation. (c) Comparison between diffusion coefficients of TEGO, H-TEGO and graphite, calculated at different stages of the lithiation process. (d) Proposed mechanism of Li diffusion in TEGO and H-TEGO.

3.4. Charge Storage Mechanisms

Two significant differences are observed between TEGO and H-TEGO. The first is the larger specific capacity of H-TEGO, calculated from GCP; the second is the diffusion coefficient of lithium in the electrode, calculated from EIS. In particular, while diffusion in TEGO is about 10 times faster than that of graphite, diffusion in H-TEGO is actually much slower: for example, about 10 times slower than graphite and 100 times slower than TEGO (Figure 4 (c)). Moreover, between lithiation and de-lithiation, a difference in the behavior of the diffusion coefficient has been observed. This is probably due to the unconventional voltage shapes of TEGO and H-TEGO, which, instead of displaying the plateau typically present in conventional graphite anodes, features a steeply decreasing behavior during discharge (lithiation) and an approximatively linear behavior during charge (de-lithiation), as seen in Figures 1 (a) and 1 (b). This hysteresis causes a significant difference in the derivative of the potential with respect to the lithium content in the electrode, while the Warburg coefficient is more regular. The hysteresis effect has been observed before in graphene-related materials, but no explanation has been given yet [18,25,49]. The effect has also been observed in hard-carbon electrodes [50,51], for which an explanation has been given, involving two different process: an intercalation process leading to linearly decreasing voltage, and a Li-C bonding process at the edge of planar aromatic carbon sheets driven by an activation energy step and leading to a voltage plateau [52]. Despite this effect has been explained only for hydrogen-edged planar aromatic carbon sheets, the fact that hysteresis is observed also in non-hydrogen-containing hard carbon suggests that it is hydrogen-favored, but not exclusive to hydrogen-edge carbon sheets.

It has been reported that charge transfer impedance of the lithium-electrolyte interface in half-cells is non-negligible and that it possesses a time constant similar to that of the anode-electrolyte charge transfer; consequently, the contribution of the charge transfer mechanisms is irresolvable [53]. However, all the half-cells tested with EIS were prepared in the same conditions, hence it is safe to assume that the contribution of the lithium-electrolyte interface is similar for each cell, thus allowing a comparison between the charge transfer impedance and diffusion coefficients of TEGO, H-TEGO and graphite. Moreover, while diffusion should be dependent on the state of charge of the anode, charge transfer resistance of lithium is theoretically independent from the state of charge: therefore, the behavior of the diffusion coefficient as a function of the state of charge is reliable. In addition to this, diffusion coefficients for TEGO and graphite are consistent with previously reported diffusion of lithium in graphite; for H-TEGO, diffusion coefficient is consistent with previously reported diffusion in graphite only in a high state of charge, while it is lower than that of graphite in a low state of charge [39,48].

The difference in diffusion coefficient between TEGO and H-TEGO is quite unexpected, since H-TEGO displayed the best performance during GCP tests, both in term of specific capacity and retention of capacity during fast charge-discharge cycles, the latter of which should denote faster diffusion dynamics. Diffusion in TEGO is higher than that in graphite since TEGO is composed by small flakes of one to few layered graphene, and lithium can rapidly move in the innermost core of the flakes by crossing the space between planes, while in graphite, to completely intercalate the bulk, the distance between the core and the edges of the planes is longer. It has also been observed that lithium ions can cross one or few layers of graphene in presence of defects [49]. In H-TEGO, diffusion between layers is probably hindered by the presence of electron-positive hydrogen or other functional groups on the surface and/or on the edges of each graphene plane. This has been observed also by means of density functional theory calculations, which explain that edge-modified graphene, terminated with either -H, -O or -OH, have a higher binding energy for lithium adsorption, but also a higher energy threshold for lithium diffusion [54]. The fast charge and discharge are then probably not caused by diffusion of lithium

inside graphene layers, which is a chemical process, but by an adsorption on the surface of graphene or inside the pores of the graphene matrix (Figure 4 (d)), which is a physical process and intrinsically faster. This explanation is supported by previous NMR studies on the insertion and extraction of sodium ions in TEGO [34]; despite the active ions are different, lithium is chemically similar to sodium, which could explain the similarity in the charge accumulation behavior. In particular, NMR performed on sodium in TEGO electrodes proved the existence of three different insertion mechanisms: one consists in the intercalation of sodium between layers, the second corresponds to the insertion inside the nanopores, and the last is attributed to the formation of the SEI, which is confirmed by the irreversibility of the process.

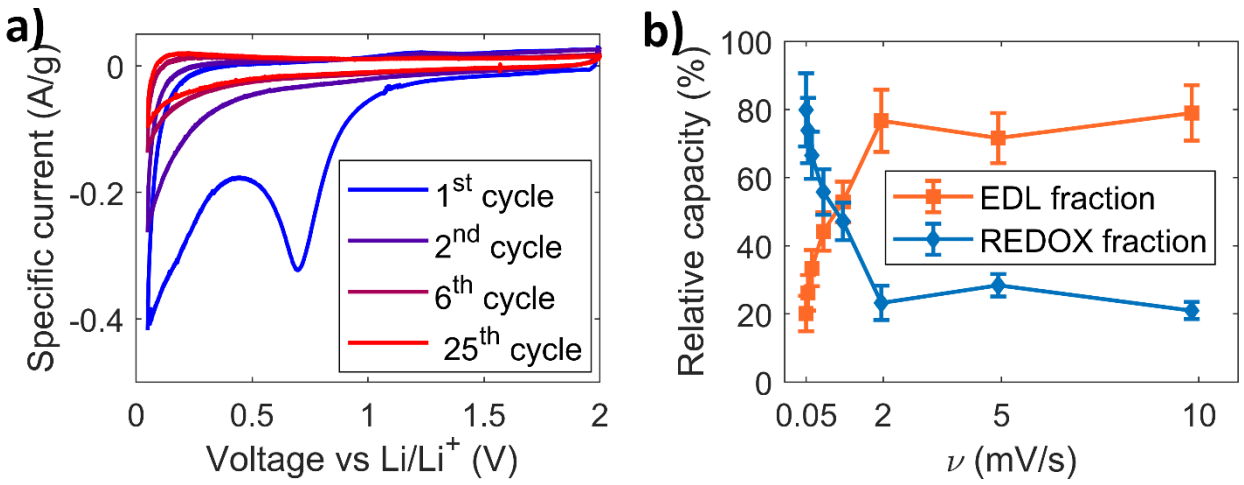

Figure 5. (a) CV performed at 100 μV/s on TEGO-based electrodes for the first 25 cycles. As observed with GCP for the first 5 cycles, CV confirms the loss of reversibility during the first 6 cycles, as well as the SEI formation during the first discharge, proven by the peak at 0.7 V in the first reduction semi-cycle. (b) Fraction of the capacity ascribable to electrostatic (Electric Double Layer, EDL) and electrochemical (redox) effects.

3.5. Cyclic Voltammetry

The physical adsorption of lithium ions on the surface of TEGO could be ascribed to the working principle of electric double-layer capacitors (EDLCs) [6,55]. In order to verify the dual nature of the energy storage mechanism in TEGO, three-electrode cyclic voltammetry (CV) was performed on fresh (without pre SEI formation) TEGO electrodes. 25 cycles at 100 μV/s were executed on a fresh TEGO electrode, to confirm the loss of reversibility already observed with GCP during the first 5 cycles. The CV curves are shown in Figure 5 (a) and essentially confirm the stability of the system after the 6th cycle, as well as the SEI formation during the first discharge, proven by the peak at 0.7 V in the first reduction semi-cycle. The increase in the absolute value of the current during reduction at low potential confirms that lithium storage in graphene mainly occurs at low potential, and a hysteresis is observed in CV, as already noted with GCP. After the formation cycles, CV measurements were performed at different voltage rates (Figure S7), in order to evaluate the electrochemical and electrostatic contributions to the total capacity with the Dunn method. Figure 5 (b) shows the fraction of the capacity ascribable to electrostatic end electrochemical effects, while Figure 6 shows the calculated contribution to the capacity, for a slow (a) and a fast (b) voltage rate. The non-ideal, triangular shape of the CV curve for a fast voltage rate (Figure 6 (b)) has been observed before for symmetrical supercapacitors [55], and is typically associated to ion sieving effects, in which the different matching between the TEGO pores size and the steric hindrance of anions and cations determines a disparity in electrical charges between the two electrodes. In our case, where one electrode is TEGO and the

other pure lithium, no ion sieving occurs, but rather the disparity of the charges is given by the fact that Li^+ ions can be hosted by the pores in the TEGO-based electrodes, while PF_6^- ions have no hosting counterpart in the lithium counter electrode.

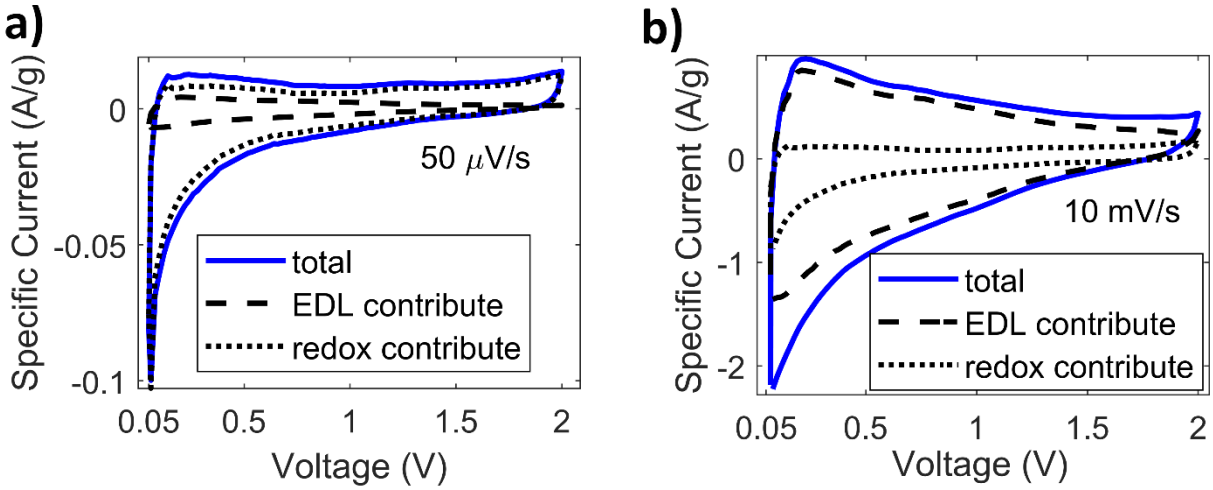

Figure 6. Calculated contribution to the capacity, for (a) a slow and (b) a fast voltage rate. Capacity is proportional to the area of the CV curve.

3.6. Double Layer Capacitance

The electrostatic capacitive charge accumulation effect, corresponding to the insertion inside the nanopores, is the explanation for the high charge and discharge rates of both TEGO and H-TEGO, and is probably not observed in the EIS characterization, since the impedance of this process is probably orders of magnitude lower than that of electrochemical intercalation. The hypothesis of the presence of a physical charge accumulation process is furtherly supported by the atypical shape of the GCP curves, which is a signature of graphene related materials-based electrodes [25]; the absence of any plateaus, and the approximatively linear GCP curve during charge, are similarities with the galvanostatic charge and discharge curves of EDLCs [55,56]. Specific capacitance calculated for TEGO and H-TEGO is actually much larger than that of typical EDLCs [56,57], but specific capacity is similar to that of batteries; for this reason, the explanation for the performance of TEGO and H-TEGO electrodes is that the fast charge and discharge rate capability is probably given by the fast, physical electrostatic charge accumulation, while the high capacity is given by the slower, electrochemical charge accumulation (Figure 4 (d)). This behavior of graphene has been already observed before [58,59], although in such cases graphene was employed only to provide the electrostatic charge accumulation, while the electrochemical charge accumulation was provided by either Mg_2Ni [58] or TiO_2 [59]; on the contrary, in our TEGO and H-TEGO based electrodes the graphene-related materials provide both the faster electrostatic accumulation and the slower electrochemical accumulation, thanks to the fact that TEGO and H-TEGO are made of both single and multiple graphene layers (up to 3-5 layers), and lithium can be electrochemically intercalated between graphene layers of few-layer layer graphene sheets. A similar effect has also been reported for ion intercalation in hard carbon [50], in anodes made from graphene exfoliated from differently oxidized graphite oxide samples [25], and for a graphene anode coupled with a graphene oxide cathode [60]. In the first case, Raman spectroscopy performed on hard carbon highlights both an intercalation mechanism, occurring at a higher voltage, and a pore occupancy mechanism, occurring at a lower voltage; the active ion is sodium, which is chemically similar to lithium [50]. The double charge storage mechanism explains the shape of the voltage discharge profile of TEGO and H-TEGO, as well as the hysteresis observed both with GCP and CV

measurements, which is explained with a double contribution to capacity. In the second case, the double nature of charge storage is proposed, but not proven [25]. In the third case, both anode and cathode were characterized by a fast surface reaction mechanism, with the advantage of more balance in power between the electrodes, but at the cost of having a much more similar potential between anode and cathode [60]; on the contrary, when TEGO and H-TEGO anodes are coupled with a commercial cathode, a higher difference in the standard potential can be achieved. However, the use of composite materials exploiting graphene as a template matrix for commercial cathode nanoparticles [61,62] is potentially beneficial to match the fast charge and discharge rates of TEGO and H-TEGO anodes, and will require further investigation.

3.7. Full-cell Characterization

Full-cells were fabricated by coupling TEGO and H-TEGO with different cathode materials. Due to the large quantity of lithium consumed by the anode during the first cycle, and due to the need to properly characterize the full-cell behavior without having to consider the Li ion loss during the first cycle, all anodes underwent a process of pre-formation of the SEI, which consists in assembling the anodes in half-cells and cycling three times, after which the anodes are removed from the half-cells and employed to assemble the full-cells. This electrochemical pre-formation method is different from previously reported direct contact with a lithium foil [20], which has the disadvantage of an incomplete formation of the electrode, proven by the capacity loss during the first cycles, indicating that more than one cycle is preferable. It was reported that the SEI was preserved after disassembling the half-cells [34]. By means of GCP, electrochemical performance of full-cells was studied. Different rates of charge and discharge were employed, in order to obtain both a good approximation of the OCV curve, and the change in capacity corresponding to high current rates. Galvanostatic potentials as a function of state of charges for full-cells with TEGO and H-TEGO based anodes at 0.1 C-rate are shown in Figures 7 (a) and 7 (b), respectively for $LiNi_{1/3}Mn_{1/3}Co_{1/3}O_2$ (NMC, Ni:Mn:Co=1:1:1) and $LiFePO_4$ (LFP) cathodes. All the cells present similar charging and discharging behaviors, highlighting the absence of evident plateaus and values of potential spanning a wide voltage range. No evident difference is observed between the potential of TEGO and H-TEGO during charge and discharge.

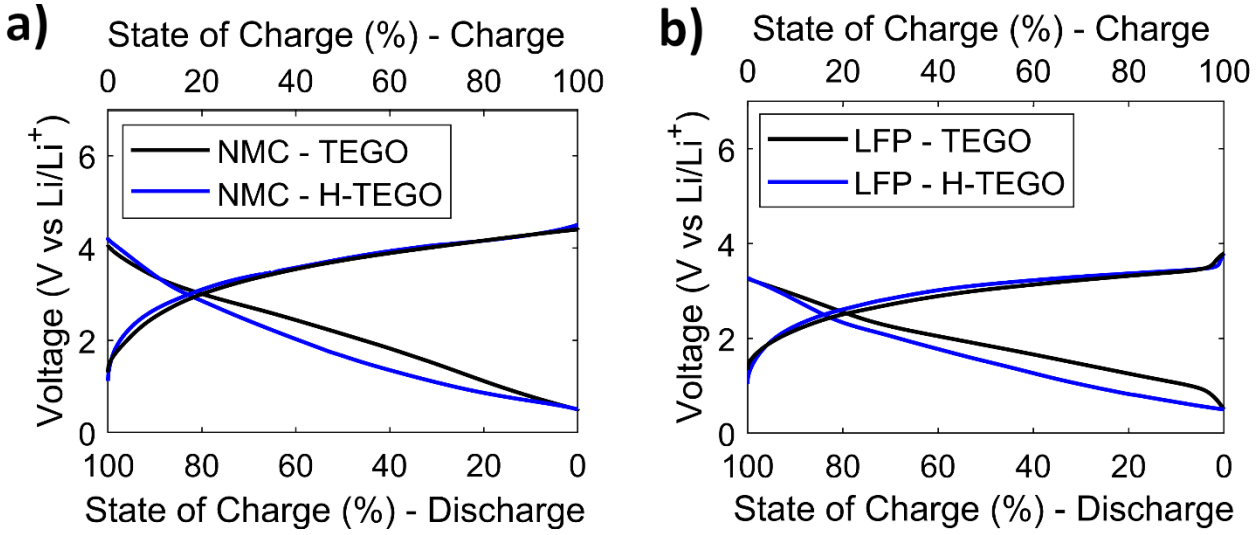

Figure 7. Voltage profiles as a function of state of charge for full-cells with either TEGO or H-TEGO anode and (a) NMC or (b) LFP cathode.

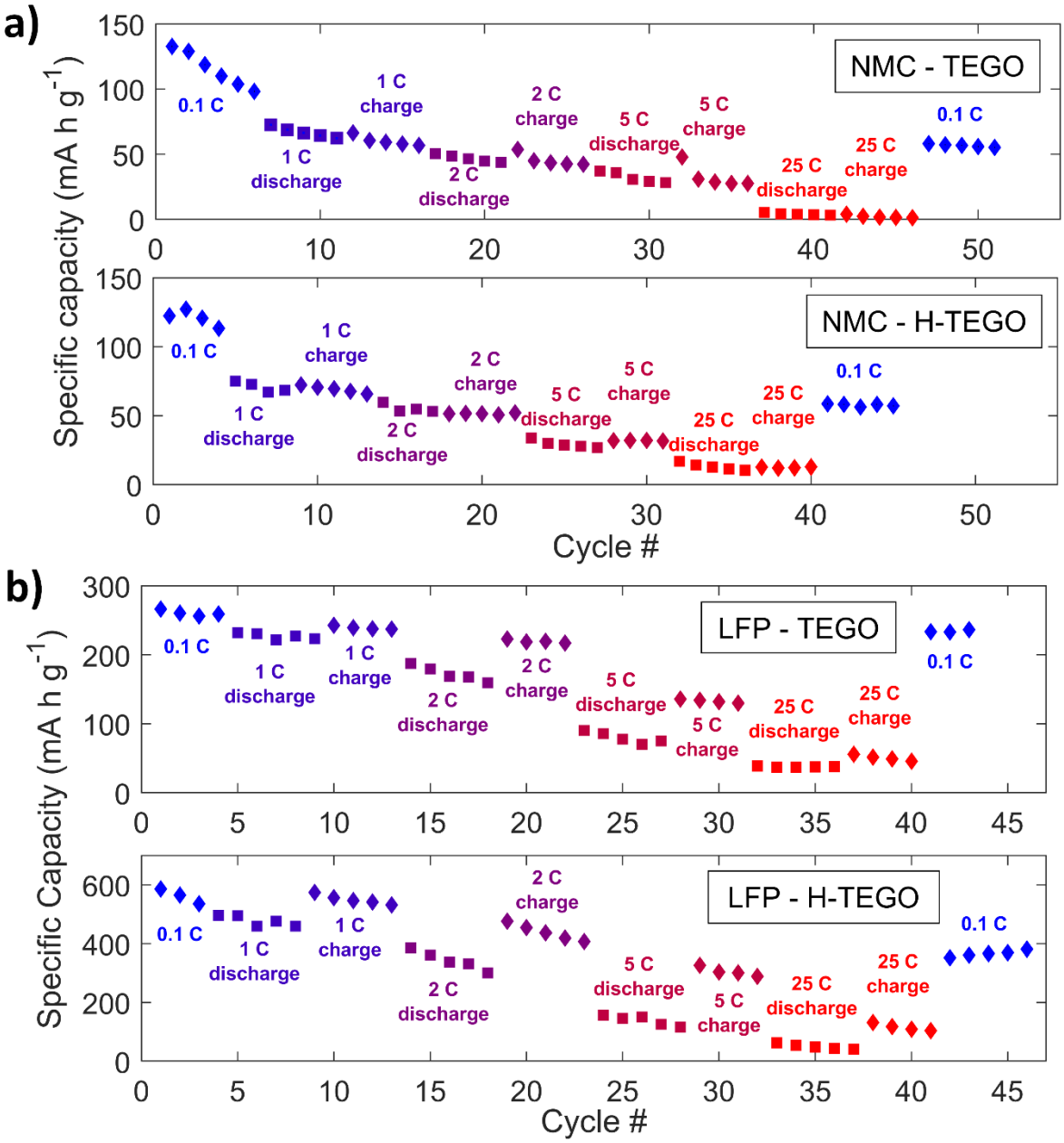

Figure 8. Specific capacities of the TEGO or H-TEGO anodes during discharge at different C-rates in full-cells made with different types of cathodes: (a) NMC or (b) LFP. Cells were either charged at a higher C-rate while keeping at 0.1 C-rate for the discharge (highlighted in the figure as "charge") or discharged at a higher C-rate while keeping at 0.1 C-rate for the charge (highlighted in the figure as "discharge).

3.7.1. NMC

Figure 8 (a) shows the discharge specific capacity of full-cells with TEGO and H-TEGO based anodes and NMC cathodes. Cells were initially charged and discharged at 0.1 C-rate, and then either charged at a higher C-rate while discharging at 0.1 C, or discharged at a higher C-rate while charging at 0.1 C. For the TEGO-based cells, a high capacity retention is observed when charging at fast C-rates, up to 5 C, and discharging at 0.1 C, while capacity drops significantly when charging at 25 C. This considerable drop in specific capacity is probably due to the limited rate capability of NMC cathode,

since fast C-rate capabilities of TEGO (as well as H-TEGO) were observed in the half-cells, with no evidence of a capacity decay as prominent as in full-cells (Figure 3 (a) and (c)). For the full-cells with electrodes based on H-TEGO and NMC, capacity retention is more stable than that of the TEGO-based full-cell, since no significant difference is observed between fast discharge and fast charge. However, specific capacity of the H-TEGO-based full-cell is lower than expected: specific capacity is similar to that of the TEGO-based full-cell, while, based on the capacity observed in the half-cells, it should be expected to be higher. A possible explanation for this behavior is that the cathode is the limiting factor, since specific capacity of the cathode is lower than expected even at the first cycles (Figure S8). This could be due to the fact that the battery is subject to a very large potential span (Figure 7 (a)), which could be harmful for the cathode and prevent its full de-lithiation. Coulombic efficiency, calculated as the average of the last few cycles at 0.1 C for both charge and discharge, was of 93% for TEGO and of 92% for H-TEGO, falling in the A^{++} category [63].

3.7.2. LFP

The GCP discharge capacity at different C-rates for full-cells with LFP cathode and either TEGO or H-TEGO anode is shown in Figure 8 (b). Cycles in which full-cells are subject to a fast charge and slow discharge show a better capacity than those in which cells are rapidly discharged and slowly charged, suggesting that, since this is not observed in NMC-based devices, the cathode is the cause of the capacity decrease. Similarly to NMC-based full-cells, the specific capacity of the cathode is lower than expected, although for LFP-based full-cells it is only a slight decrease with respect to the expected capacity (Figure S10). This could be due to the fact that the potential excursion in LFP-based cells is lower than that of NMC-based cells (Figure 7 (b)), only barely influencing the proper de-lithiation of the cathode. The full-cell with H-TEGO anode and LFP cathode features the best performance among all the full-cells that have been studied, with an anodic specific capacity of 366±11 mA h g^{-1} at low charge and discharge rate, and a still high 305±16 mA h g^{-1} when charging at 5 C, although performance drops significantly at 25 C, probably due to a limit of the cathode, as observed in all the full-cells. After a few cycles at 25 C, tests at 0.1 C show a partial recover of the initial capacity, and an increasing trend in the capacity for the subsequent cycles, indicating stability in the cycle life at slow C-rates, even after fast charge and discharge. Coulombic efficiency, calculated as the average of the last few cycles at 0.1 C for both charge and discharge, was of 94% for TEGO and of 87% for H-TEGO, falling in the A^{++} and A^{+} categories, respectively [63]. It is worth noting that, since both full-cells based on TEGO and H-TEGO have yet to recover full capacity after the cycles at 25C, actual efficiencies are probably higher than the reported ones.

3.8. TEGO and H-TEGO for Commercial Batteries

Full-cells with TEGO and H-TEGO anodes are characterized by a surprising absence of plateaus, which should be expected when coupling an anode with commercial cathodes; plateaus should be at 3.8 V for NMC and 3.4 V for LFP. Instead, cells seem to be fully charged at the same potential as the theoretical plateau potential of the cathode; their potential keeps on decreasing up to a lower limit of 1 V. This is due to the fact that the open circuit voltage of the cell is dominated by the potential of the anode, as observed for the GCP curves of the TEGO and H-TEGO half-cells. This might be an issue for application to electric traction, as the significant drop in the pack voltage when cells are being discharged might lead the Battery Management System (BMS) to reduce the power demand, hence limiting the vehicle performance.

Before exploiting TEGO or H-TEGO in commercial batteries, three main issues must be addressed. Firstly, graphene-related materials, due to their high specific surface area, give rise to a massive SEI [34]. Besides the resulting waste of

lithium, removing a large quantity of lithium from the electrolyte can cause a faster ageing of the battery, so further studies on ageing effect on graphene electrodes are needed. The second issue is that a higher-than-normal variance of the specific capacity of the electrodes is observed. This could be due to the hand-made nature of the cells; however, it could also be caused by intrinsic inhomogeneities of the electrode materials. Lastly and more importantly, the main issue is the slope of the OCV curve, which does not present plateaus, but rather a surprising hysteresis, with an almost linear behavior during discharge, typical for supercapacitors, and a steeply increasing behavior during charge, which could be the result of a combination of double-layer capacitance and redox effects. Such behavior is typically avoided in batteries, but it could also be the solution to some typical problems of existing technologies. The first is the fact that plateau potential of graphite is very close to zero versus Li/Li^+; this may cause the formation of a metallic lithium plating on the anode as typically happens when charging and discharging the battery at high current rates due to the potential drop caused by the internal resistance of the battery [64]. The second is the fact that some cathode materials, among which LFP, has a very flat plateau in the OCV curve, which makes it hard to estimate the state of charge of the battery from current and voltage measurements. For LFP in particular, the maximal corresponding rate of change in SOC is as high as 4% per mV for most of the discharge curve [65], without even taking into account potential changes due to temperature changes, drift currents and ageing [66]. These two problems could be addressed by using TEGO or H-TEGO as negative electrode materials, but the issue of the non-flat potential must be solved. One strategy is that of assembling a battery with an unbalanced ratio of cathode and anode: for example, if the graphene needed to balance the capacity of the cathode is doubled, its contribution to the potential difference of the cell is halved; the potential range of the battery can also be controlled by assembling the battery with graphene in a partially lithiated stage, so that the potential difference of the cell is always in the higher half. The proposed method for pre-lithiation grants enough control on the level of lithiation of the anode material, to tune the exact state of charge needed before assembling the full-cell. Lastly, it has been observed that cathodes, due to their lower rate of charge and discharge capabilities, hinder the high current capabilities of TEGO and H-TEGO; such effect is less evident in LFP, especially during charge. This power imbalance could be solved by developing proper cathodes with higher C-rate capabilities, such as composites of metal oxide nanoparticles in a carbon matrix [61,62], and it will require further investigation.

4. Conclusions

Graphene synthesized with a scalable method based on thermal exfoliation of graphite oxide in controlled atmosphere was effectively employed and characterized as anode material in LIBs, to better understand the intercalation mechanism and to develop a more performing technology for LIBs. Graphene was also hydrogenated, to remove oxygen atoms and saturate dangling bonds, with the result of enhancing its properties for LIBs. Moreover, for the first time, graphene produced by thermal exfoliation and hydrogenated graphene were coupled to commercial cathodes, in order to develop complete cell prototypes to evaluate the anode performance in a setting similar to a possible commercially viable product.

The electrochemical intercalation of lithium in thermally exfoliated graphite oxide (TEGO) and hydrogenated TEGO (H-TEGO) was investigated by realizing and characterizing half-cells with anodes based on TEGO and H-TEGO. Lithium was successfully intercalated in TEGO, with a reversible specific capacity of 304 mA h g^{-1} at 0.1 C. TEGO proved to be especially good for its high charge and discharge rate capabilities, retaining nearly 36% of capacity even at an extreme C-rate of 25 C, both during charge and discharge. H-TEGO featured an even more outstanding performance, with a reversible specific capacity of 1290 mA h g^{-1} at 0.1 C, of 670 mA h g^{-1} at 1 C-rate and of 360 mA h g^{-1} at 25 C-rate.

Diffusion of lithium ions in TEGO and H-TEGO was studied with EIS analysis. For the first time, diffusion of lithium in graphene and hydrogenated graphene has been studied at different concentrations of lithium in the electrodes, both during lithiation and de-lithiation. A diffusion coefficient of about $2 \cdot 10^{-8}$ cm^2 s^{-1} at 50% SOC, about 10 times higher than that of graphite, was calculated for TEGO, while a diffusion coefficient of $1 \cdot 10^{-10}$ cm^2 s^{-1} at 50% SOC was calculated for H-TEGO.

The simultaneous occurrence of two distinct charge storage phenomena was suggested by the atypical shape of the GCP curves, along with the fact that H-TEGO, while being capable of faster charging and discharging with respect to TEGO, was also characterized by slower intercalation dynamics. Three-electrode CV measurements further corroborated the coexistence of two distinct charge storage mechanisms: battery-like electrochemical intercalation, due to lithium insertion between graphene layers and responsible of the high capacity, and supercapacitor-like electrostatic accumulation of charges, due to lithium adsorbed into graphene pores or attracted by electrical charges on graphene surface and responsible of the fast charge and discharge capabilities. To the best of our knowledge, it is the first time in which this effect is reported and explained for pristine graphene in lihium-ion batteries. For the first time graphene, produced with a highly scalable thermal exfoliation, with the added advantage of not requiring the use of heavy metals in the synthesis process, and hydrogenated graphene have been coupled to a cathode in full-cells, which were studied by means of GCP; either lithium nickel manganese cobalt oxide (NMC) or lithium iron phosphate (LFP) have been employed as cathodes. The best performance has been obtained for full-cells with LFP, and in particular for the cell coupling H-TEGO with LFP, probably due to the faster rate capabilities of the cathode, with an anodic specific capacity of 305 mA h g^{-1} at 5 C-rate. Such a good performance makes graphene a very interesting candidate as anode for lithium-ion batteries.

Acknowledgements

The authors acknowledge financial support from the European Social Fund (Emilia-Romagna FSE 2014/2020 program, project number 2019-12772/RER, 'Parma E-lab – Parma Entrepreneurship Lab') and Cariplo Foundation (project number 2019-2152, 'Gaining health and energy from Lombard agrifood waste'). The experimental work presented in this paper was in part conducted with support from the National Science Foundation (Award No. CMMI-1554063). The authors acknowledge Dr. Francesca Ridi of University of Firenze for the BET analysis. The authors acknowledge Lalith Rao and Dr. Ke Pan for the experimental support and useful discussion.

Data Availability

The raw/processed data required to reproduce these findings cannot be shared at this time as the data also forms part of an ongoing study.

References

[1] J.M. Tarascon, M. Armand, Issues and challenges facing rechargeable lithium batteries, Nature. 414 (2001) 359–367. https://doi.org/10.1038/35104644.

[2] J. Akridge, R. Brodd, Li-ion Markets, Pacific Power Symp. (2010).

[3] Panasonic Industrial Devices, Battery Product Safety Data Sheet - NCR18650PF, (2021). https://industrial.panasonic.com.

[4] X. Zhu, Z. Guo, Z. Hou, Solar-powered airplanes: A historical perspective and future challenges, Prog. Aerosp.

Sci. 71 (2014) 36–53. https://doi.org/10.1016/j.paerosci.2014.06.003.

[5] V.B. Mohan, K. Jayaraman, D. Bhattacharyya, Brunauer–Emmett–Teller (BET) specific surface area analysis of different graphene materials: A comparison to their structural regularity and electrical properties, Solid State Commun. 320 (2020). https://doi.org/10.1016/j.ssc.2020.114004.

[6] Y. Gao, Graphene and polymer composites for supercapacitor applications: A review, Nanoscale Res. Lett. 12 (2017). https://doi.org/10.1186/s11671-017-2150-5.

[7] D. Pontiroli, S. Scaravonati, G. Magnani, L. Fornasini, D. Bersani, G. Bertoni, C. Milanese, A. Girella, F. Ridi, R. Verucchi, L. Mantovani, A. Malcevschi, M. Riccò, Super-activated biochar from poultry litter for high-performance supercapacitors, Microporous Mesoporous Mater. 285 (2019) 161–169. https://doi.org/10.1016/j.micromeso.2019.05.002.

[8] A.N. Zaderko, L.M. Grishchenko, D. Pontiroli, S. Scaravonati, M. Riccò, V.E. Diyuk, V.A. Skryshevsky, V. V. Lisnyak, Enhancing the performance of carbon electrodes in supercapacitors through medium-temperature fluoroalkylation, Appl. Nanosci. (2021). https://doi.org/10.1007/s13204-020-01651-0.

[9] P. Lian, X. Zhu, S. Liang, Z. Li, W. Yang, H. Wang, Large reversible capacity of high quality graphene sheets as an anode material for lithium-ion batteries, Electrochim. Acta. 55 (2010) 3909–3914. https://doi.org/10.1016/j.electacta.2010.02.025.

[10] S.K. Vashist, A.G. Venkatesh, Advances in graphene-based sensors and devices, J. Nanomedicine Nanotechnol. 4 (2013). https://doi.org/10.4172/2157-7439.1000e127.

[11] R.O. Loutfy, S. Katagiri, Fullerene Materials for Lithium-ion Battery Applications, in: Perspect. Fuller. Nanotechnol., 2002: pp. 357–367. https://doi.org/10.1007/978-94-010-9598-3_32.

[12] J.A. Teprovich, J.A. Weeks, P.A. Ward, S.C. Tinkey, C. Huang, J. Zhou, R. Zidan, P. Jena, Hydrogenated C60 as High-Capacity Stable Anode Materials for Li Ion Batteries, ACS Appl. Energy Mater. 2 (2019) 6453–6460. https://doi.org/10.1021/acsaem.9b01040.

[13] S. Scaravonati, G. Magnani, M. Gaboardi, G. Allodi, M. Riccò, D. Pontiroli, Electrochemical intercalation of fullerene and hydrofullerene with sodium, Carbon N. Y. 130 (2018) 11–18. https://doi.org/10.1016/j.carbon.2017.12.107.

[14] D. Pontiroli, S. Scaravonati, M. Sidoli, G. Magnani, L. Fornasini, C. Milanese, M. Riccò, Fullerene mixtures as negative electrodes in innovative Na-ion batteries, Chem. Phys. Lett. 731 (2019). https://doi.org/10.1016/j.cplett.2019.136607.

[15] S. Ren, P. Rong, Q. Yu, Preparations, properties and applications of graphene in functional devices: A concise review, Ceram. Int. 44 (2018) 11940–11955. https://doi.org/10.1016/j.ceramint.2018.04.089.

[16] W. Jiang, H. Wang, Z. Xu, N. Li, C. Chen, C. Li, J. Li, H. Lv, L. Kuang, X. Tian, A review on manifold synthetic and reprocessing methods of 3D porous graphene-based architecture for Li-ion anode, Chem. Eng. J. 335 (2018) 954–969. https://doi.org/10.1016/j.cej.2017.11.020.

[17] Xiaoyi Cai, Linfei Lai, Zexiang Shen, Jianyi Lin, Graphene and graphene-based composites as Li-ion battery electrode materials and their application in full cells, J. Mater. Chem. A. 5 (2017) 15423–15446. https://doi.org/10.1039/C7TA04354F.

[18] J.C. Pramudita, D. Pontiroli, G. Magnani, M. Gaboardi, M. Riccò, C. Milanese, H.E.A. Brand, N. Sharma, Graphene and Selected Derivatives as Negative Electrodes in Sodium- and Lithium-Ion Batteries, ChemElectroChem. 2 (2015) 600–610. https://doi.org/10.1002/celc.201402352.

[19] L. Fornasini, S. Scaravonati, G. Magnani, A. Morenghi, M. Sidoli, D. Bersani, G. Bertoni, L. Aversa, R.

Verucchi, M. Riccò, P.P. Lottici, D. Pontiroli, In situ decoration of laser-scribed graphene with TiO2 nanoparticles for scalable high-performance micro-supercapacitors, Carbon N. Y. 176 (2021) 296–306. https://doi.org/10.1016/j.carbon.2021.01.129.

[20] J. Hassoun, F. Bonaccorso, M. Agostini, M. Angelucci, M.G. Betti, R. Cingolani, M. Gemmi, C. Mariani, S. Panero, V. Pellegrini, B. Scrosati, An advanced lithium-ion battery based on a graphene anode and a lithium iron phosphate cathode, Nano Lett. 14 (2014) 4901–4906. https://doi.org/10.1021/nl502429m.

[21] Z. Zhang, C. Zhou, L. Huang, X. Wang, Y. Qu, Y. Lai, J. Li, Synthesis of bismuth sulfide/reduced graphene oxide composites and their electrochemical properties for lithium ion batteries, Electrochim. Acta. 114 (2013) 88–94. https://doi.org/10.1016/j.electacta.2013.09.174.

[22] J.G. Ren, Q.H. Wu, H. Tang, G. Hong, W. Zhang, S.T. Lee, Germanium-graphene composite anode for high-energy lithium batteries with long cycle life, J. Mater. Chem. A. 1 (2013) 1821–1826. https://doi.org/10.1039/c2ta01286c.

[23] M. Su, S. Liu, L. Tao, Y. Tang, A. Dou, J. Lv, Y. Liu, Silicon@graphene composite prepared by spray–drying method as anode for lithium ion batteries, J. Electroanal. Chem. 844 (2019) 86–90. https://doi.org/10.1016/j.jelechem.2019.04.072.

[24] Y. Yang, B. Qiao, X. Yang, L. Fang, C. Pan, W. Song, H. Hou, X. Ji, Lithium titanate tailored by cathodically induced graphene for an ultrafast lithium ion battery, Adv. Funct. Mater. 24 (2014) 4349–4356. https://doi.org/10.1002/adfm.201304263.

[25] H.F. Xiang, Z.D. Li, K. Xie, J.Z. Jiang, J.J. Chen, P.C. Lian, J.S. Wu, Y. Yu, H.H. Wang, Graphene sheets as anode materials for Li-ion batteries: Preparation, structure, electrochemical properties and mechanism for lithium storage, RSC Adv. 2 (2012) 6792–6799. https://doi.org/10.1039/c2ra20549a.

[26] W. Wang, H. Cao, X. Zhou, Z. Liu, Synthesis of graphene, 2014. https://doi.org/10.1201/b17757.

[27] N.I. Zaaba, K.L. Foo, U. Hashim, S.J. Tan, W.W. Liu, C.H. Voon, Synthesis of Graphene Oxide using Modified Hummers Method: Solvent Influence, in: Procedia Eng., 2017: pp. 469–477. https://doi.org/10.1016/j.proeng.2017.04.118.

[28] M. Gaboardi, A. Bliersbach, G. Bertoni, M. Aramini, G. Vlahopoulou, D. Pontiroli, P. Mauron, G. Magnani, G. Salviati, A. Züttel, M. Riccò, Decoration of graphene with nickel nanoparticles: Study of the interaction with hydrogen, J. Mater. Chem. A. 2 (2014) 1039–1046. https://doi.org/10.1039/c3ta14127f.

[29] C. Li, X. Zhang, K. Wang, X. Sun, Y. Ma, High-power lithium-ion hybrid supercapacitor enabled by holey carbon nanolayers with targeted porosity, J. Power Sources. 400 (2018) 468–477. https://doi.org/10.1016/J.JPOWSOUR.2018.08.013.

[30] C. Li, X. Zhang, K. Wang, X. Sun, G. Liu, J. Li, H. Tian, J. Li, Y. Ma, C. Li, X. Zhang, K. Wang, X. Sun, Y. Ma, G. Liu, J. Li, H. Tian, Scalable Self-Propagating High-Temperature Synthesis of Graphene for Supercapacitors with Superior Power Density and Cyclic Stability, Adv. Mater. 29 (2017) 1604690. https://doi.org/10.1002/ADMA.201604690.

[31] C. Li, X. Zhang, K. Wang, X. Sun, Y. Xu, F. Su, C.M. Chen, F. Liu, Z.S. Wu, Y. Ma, Nitrogen-enriched graphene framework from a large-scale magnesiothermic conversion of CO2 with synergistic kinetics for high-power lithium-ion capacitors, NPG Asia Mater. 2021 131. 13 (2021) 1–16. https://doi.org/10.1038/s41427-021-00327-7.

[32] C. Li, X. Zhang, K. Wang, X. Sun, Y. Ma, High-power and long-life lithium-ion capacitors constructed from N-doped hierarchical carbon nanolayer cathode and mesoporous graphene anode, Carbon N. Y. 140 (2018) 237–

248. https://doi.org/10.1016/J.CARBON.2018.08.044.

[33] J.C. Pramudita, D. Pontiroli, G. Magnani, M. Gaboardi, C. Milanese, G. Bertoni, N. Sharma, M. Riccò, Effect of Ni-nanoparticles decoration on graphene to enable high capacity sodium-ion battery negative electrodes, Electrochim. Acta. 250 (2017) 212–218. https://doi.org/10.1016/j.electacta.2017.08.049.

[34] J.C. Pramudita, A. Rawal, M. Choucair, D. Pontiroli, G. Magnani, M. Gaboardi, M. Riccò, N. Sharma, Mechanisms of sodium insertion/extraction on the surface of defective graphenes, ACS Appl. Mater. Interfaces. 9 (2017) 431–438. https://doi.org/10.1021/acsami.6b13104.

[35] C. Cavallari, D. Pontiroli, M. Jiménez-Ruiz, A. Ivanov, M. Mazzani, M. Gaboardi, M. Aramini, M. Brunelli, M. Riccò, S. Rols, Hydrogen on graphene investigated by inelastic neutron scattering, J. Phys. Conf. Ser. 554 (2014) 012009. https://doi.org/10.1088/1742-6596/554/1/012009.

[36] C. Ho, I.D. Raistrick, R.A. Huggins, Application of A-C Techniques to the Study of Lithium Diffusion in Tungsten Trioxide Thin Films, J. Electrochem. Soc. 127 (1980) 343–350. https://doi.org/10.1149/1.2129668.

[37] M. Winter, G.H. Wrodnigg, J.O. Besenhard, W. Biberacher, P. Novák, Dilatometric Investigations of Graphite Electrodes in Nonaqueous Lithium Battery Electrolytes, J. Electrochem. Soc. 147 (2000) 2427. https://doi.org/10.1149/1.1393548.

[38] S. Schweidler, L. De Biasi, A. Schiele, P. Hartmann, T. Brezesinski, J. Janek, Volume Changes of Graphite Anodes Revisited: A Combined Operando X-ray Diffraction and in Situ Pressure Analysis Study, J. Phys. Chem. C. 122 (2018) 8829–8835. https://doi.org/10.1021/acs.jpcc.8b01873.

[39] M.D. Levi, D. Aurbach, Diffusion coefficients of lithium ions during intercalation into graphite derived from the simultaneous measurements and modeling of electrochemical impedance and potentiostatic intermittent titration characteristics of thin graphite electrodes, J. Phys. Chem. B. 101 (1997) 4641–4647. https://doi.org/10.1021/jp9701911.

[40] K. Pan, F. Zou, M. Canova, Y. Zhu, J.H. Kim, Systematic electrochemical characterizations of Si and SiO anodes for high-capacity Li-Ion batteries, J. Power Sources. 413 (2019) 20–28. https://doi.org/10.1016/j.jpowsour.2018.12.010.

[41] H. Yang, H.J. Bang, J. Prakash, Evaluation of Electrochemical Interface Area and Lithium Diffusion Coefficient for a Composite Graphite Anode, J. Electrochem. Soc. 151 (2004) A1247. https://doi.org/10.1149/1.1763139.

[42] N. Ding, J. Xu, Y.X. Yao, G. Wegner, X. Fang, C.H. Chen, I. Lieberwirth, Determination of the diffusion coefficient of lithium ions in nano-Si, Solid State Ionics. 180 (2009) 222–225. https://doi.org/10.1016/j.ssi.2008.12.015.

[43] S.H. Nguyen, J.C. Lim, J.K. Lee, Electrochemical characteristics of bundle-type silicon nanorods as an anode material for lithium ion batteries, Electrochim. Acta. 74 (2012) 53–58. https://doi.org/10.1016/j.electacta.2012.03.176.

[44] J. Wang, J. Polleux, J. Lim, B. Dunn, Pseudocapacitive contributions to electrochemical energy storage in TiO 2 (anatase) nanoparticles, J. Phys. Chem. C. 111 (2007) 14925–14931. https://doi.org/10.1021/jp074464w.

[45] T. Brezesinski, J. Wang, J. Polleux, B. Dunn, S.H. Tolbert, Templated nanocrystal-based porous TiO2 films for next-generation electrochemical capacitors, J. Am. Chem. Soc. 131 (2009) 1802–1809. https://doi.org/10.1021/ja8057309.

[46] D. Pontiroli, M. Aramini, M. Gaboardi, M. Mazzani, S. Sanna, F. Caracciolo, P. Carretta, C. Cavallari, S. Rols, R. Tatti, L. Aversa, R. Verucchi, M. Riccò, Tracking the hydrogen motion in defective graphene, J. Phys.

Chem. C. 118 (2014) 7110–7116. https://doi.org/10.1021/jp408339m.

[47] C. Cavallari, S. Rols, H.E. Fischer, M. Brunelli, M. Gaboardi, G. Magnani, M. Riccò, D. Pontiroli, Neutron scattering study of nickel decorated thermally exfoliated graphite oxide, Int. J. Hydrogen Energy. 44 (2019) 30999–31007. https://doi.org/10.1016/j.ijhydene.2019.09.226.

[48] M.D. Levi, C. Wang, J.S. Gnanaraj, D. Aurbach, Electrochemical behavior of graphite anode at elevated temperatures in organic carbonate solutions, in: J. Power Sources, 2003: pp. 538–542. https://doi.org/10.1016/S0378-7753(03)00279-9.

[49] F. Yao, F. Güneş, H.Q. Ta, S.M. Lee, S.J. Chae, K.Y. Sheem, C.S. Cojocaru, S.S. Xie, Y.H. Lee, Diffusion mechanism of lithium ion through basal plane of layered graphene, J. Am. Chem. Soc. 134 (2012) 8646–8654. https://doi.org/10.1021/ja301586m.

[50] J.S. Weaving, A. Lim, J. Millichamp, T.P. Neville, D. Ledwoch, E. Kendrick, P.F. McMillan, P.R. Shearing, C.A. Howard, D.J.L. Brett, Elucidating the sodiation mechanism in hard carbon by operando raman spectroscopy, ACS Appl. Energy Mater. 3 (2020) 7474–7484. https://doi.org/10.1021/acsaem.0c00867.

[51] Y. Saito, K. Takano, K. Kanari, K. Nozaki, Voltage hysteresis and heat generation behavior in lithium-ion batteries, in: Mater. Res. Soc. Symp. - Proc., 1998: pp. 551–556. https://doi.org/10.1557/proc-496-551.

[52] T. Zheng, W.R. McKinnon, J.R. Dahn, Hysteresis during Lithium Insertion in Hydrogen-Containing Carbons, J. Electrochem. Soc. 143 (1996) 2137–2145. https://doi.org/10.1149/1.1836972.

[53] T.S. Ong, H. Yang, Symmetrical cell for electrochemical AC impedance studies of lithium intercalation into graphite, Electrochem. Solid-State Lett. 4 (2001). https://doi.org/10.1149/1.1373377.

[54] E.G. Leggesse, C.L. Chen, J.C. Jiang, Lithium diffusion in graphene and graphite: Effect of edge morphology, Carbon N. Y. 103 (2016) 209–216. https://doi.org/10.1016/j.carbon.2016.03.016.

[55] F. Béguin, V. Presser, A. Balducci, E. Frackowiak, Carbons and electrolytes for advanced supercapacitors, Adv. Mater. 26 (2014) 2219–2251. https://doi.org/10.1002/adma.201304137.

[56] G.Z. Chen, Understanding supercapacitors based on nano-hybrid materials with interfacial conjugation, Prog. Nat. Sci. Mater. Int. 23 (2013) 245–255. https://doi.org/10.1016/j.pnsc.2013.04.001.

[57] P. Simon, Y. Gogotsi, B. Dunn, Where do batteries end and supercapacitors begin?, Science (80). 343 (2014) 1210–1211. https://doi.org/10.1126/science.1249625.

[58] N. Li, Y. Du, Q.P. Feng, G.W. Huang, H.M. Xiao, S.Y. Fu, A Novel Type of Battery-Supercapacitor Hybrid Device with Highly Switchable Dual Performances Based on a Carbon Skeleton/Mg2Ni Free-Standing Hydrogen Storage Electrode, ACS Appl. Mater. Interfaces. 9 (2017) 44828–44838. https://doi.org/10.1021/acsami.7b14271.

[59] H. Kim, M.Y. Cho, M.H. Kim, K.Y. Park, H. Gwon, Y. Lee, K.C. Roh, K. Kang, A novel high-energy hybrid supercapacitor with an anatase tio 2-reduced graphene oxide anode and an activated carbon cathode, Adv. Energy Mater. 3 (2013) 1500–1506. https://doi.org/10.1002/aenm.201300467.

[60] H. Kim, K.Y. Park, J. Hong, K. Kang, All-graphene-battery: Bridging the gap between supercapacitors and lithium ion batteries, Sci. Rep. 4 (2014). https://doi.org/10.1038/srep05278.

[61] A. Guler, H. Gungor, S. Ozcan, A. Coban, M.O. Guler, H. Akbulut, A high-performance composite positive electrode based on graphene and Li (Ni1/3Co1/3Mn1/3)O2, Int. J. Energy Res. 42 (2018) 4499–4511. https://doi.org/10.1002/er.4198.

[62] G. Longoni, J.K. Panda, L. Gagliani, R. Brescia, L. Manna, F. Bonaccorso, V. Pellegrini, In situ LiFePO4 nano-particles grown on few-layer graphene flakes as high-power cathode nanohybrids for lithium-ion batteries,

Nano Energy. 51 (2018) 656–667. https://doi.org/10.1016/j.nanoen.2018.07.013.

[63] P. Meister, H. Jia, J. Li, R. Kloepsch, M. Winter, T. Placke, Best Practice: Performance and Cost Evaluation of Lithium Ion Battery Active Materials with Special Emphasis on Energy Efficiency, Chem. Mater. 28 (2016) 7203–7217. https://doi.org/10.1021/ACS.CHEMMATER.6B02895/SUPPL_FILE/CM6B02895_SI_001.PDF.

[64] C. Uhlmann, J. Illig, M. Ender, R. Schuster, E. Ivers-Tiffée, In situ detection of lithium metal plating on graphite in experimental cells, J. Power Sources. 279 (2015) 428–438. https://doi.org/10.1016/j.jpowsour.2015.01.046.

[65] L. Lu, X. Han, J. Li, J. Hua, M. Ouyang, A review on the key issues for lithium-ion battery management in electric vehicles, J. Power Sources. 226 (2013) 272–288. https://doi.org/10.1016/j.jpowsour.2012.10.060.

[66] Y. Wang, C. Zhang, Z. Chen, A method for state-of-charge estimation of LiFePO4 batteries at dynamic currents and temperatures using particle filter, J. Power Sources. 279 (2015) 306–311. https://doi.org/10.1016/j.jpowsour.2015.01.005.